A&A 423, 737–744 (2004)
DOI: 10.1051/0004-6361:20034542

Astronomy & Astrophysics

Phase diversity restoration of sunspot images

I. Relations between penumbral and photospheric features

J. A. Bonet[1], I. Márquez[1,4], R. Muller[2], M. Sobotka[3], and A. Tritschler[5,6]

[1] Instituto de Astrofísica de Canarias, 38205 La Laguna, Tenerife, Spain
[2] Observatoire du Pic du Midi, 57 avenue d'Azereix, BP 826, 65008 Tarbes, France
[3] Astronomical Institute, Academy of Sciences of the Czech Republic, 25165 Ondřejov, Czech Republic
[4] Departamento de Análisis Matemático de la Universidad de La Laguna, 38271 La Laguna, Tenerife, Spain
[5] Kiepenheuer-Institut für Sonnenphysik, Schöneckstr. 6, 79104 Freiburg, Germany
[6] Big bear Solar Observatory, New Jersey Institute of Technology, 40386 North Shore Lane, Big Bear City, CA-92314, USA

Received 20 October 2003 / Accepted 30 April 2004

Abstract. We investigate the dynamics of and the relations between small-scale penumbral and photospheric features near the outer penumbral boundary: penumbral grains (PGs), dark penumbral fibrils, granules, and photospheric *G*-band bright points. The analysis is based on a 2 h time sequence of a sunspot close to disc center, taken simultaneously in the *G*-band and in the blue continuum at 450.7 nm. Observations were performed at the Swedish Vacuum Solar Telescope (La Palma) in July 1999. A total of 2564 images (46″×75″) were corrected for telescope aberrations and turbulence perturbations by applying the inversion method of phase diversity. Our findings can by summarized as follows: (a) one third of the outward-moving PGs pass through the outer penumbral boundary and then either continue moving as small bright features or expand and develop into granules. (b) Former PGs and *G*-band bright points next to the spot reveal a different nature. The latter have not been identified as a continuation of PGs escaping from the penumbra. The *G*-band bright points are mostly born close to dark penumbral fibrils where the magnetic field is strong, whereas PGs stem from the less-magnetized penumbral component and evolve presumably to non-magnetic granules or small bright features.

Key words. Sun: photosphere – Sun: sunspots – methods: data analysis – techniques: image processing

1. Introduction

The magnetic field generated at the bottom of the convection zone emerges in active regions, from where it is diffused to the surface of the Sun, by convective motions and large scale plasma circulation. However, the mechanism by which magnetic flux is taken away from sunspots is not well known yet. The aim of this work is to investigate how the features inside and outside the penumbra of a decaying sunspot are related. Decaying sunspots are well suited for that purpose, because it is believed that the decay of a sunspot proceeds predominantly by erosion of its perimeter leading to a quadratic decay law (Sheeley 1972; Meyer et al. 1974; Petrovay & Moreno-Insertis 1997).

Sunspots are very complex magnetic structures, embedded in a convective plasma, which show a small-scale pattern, down to the resolution limit of the largest contemporary solar telescopes (~0.″1 = 75 km). The surrounding convective plasma is mainly observed in the form of granules. However, the granular convection is perturbed by the presence of many magnetic elements, visible in *G*-band as tiny bright points located in intergranular spaces. They correspond to the facular and magnetic elements which are visible in lower resolution filtergrams and magnetograms. The granules (Muller & Ména 1987; Simon et al. 1988) and the magnetic elements – either observed in filtergrams or in magnetograms – (Sheeley 1969, 1972; Sheeley & Bhatnagar 1971; Vrabec 1971, 1974; Harvey & Harvey 1973; Muller & Ména 1987; Brickhouse & La Bonte 1988; Lee 1992; Ryutova et al. 1998) move radially outwards, through an annular cell. This annular cell has been called a "moat" and the magnetic elements, moving accross, "moving magnetic features" or "MMFs" (Sheeley 1972; Harvey & Harvey 1973). Dopplergrams have shown that this outflow, with speed of 0.5−1.0 km s^{-1}, is very similar to that observed in supergranules. This has suggested that the moat is presumably a supergranule whose center is occupied by a sunspot, and which extends approximately 10 000 km beyond the spot's edge (Sheeley 1972). The penumbra-granulation boundary appears very sharp, since the photospheric features (granules and bright points) are directly adjacent to darker penumbral elements (dark diffuse patches, dark and bright fibrils).

The penumbra has a very complex morphological, magnetic and dynamic structure, which is not yet properly understood physically. Visually, with the spatial resolution of

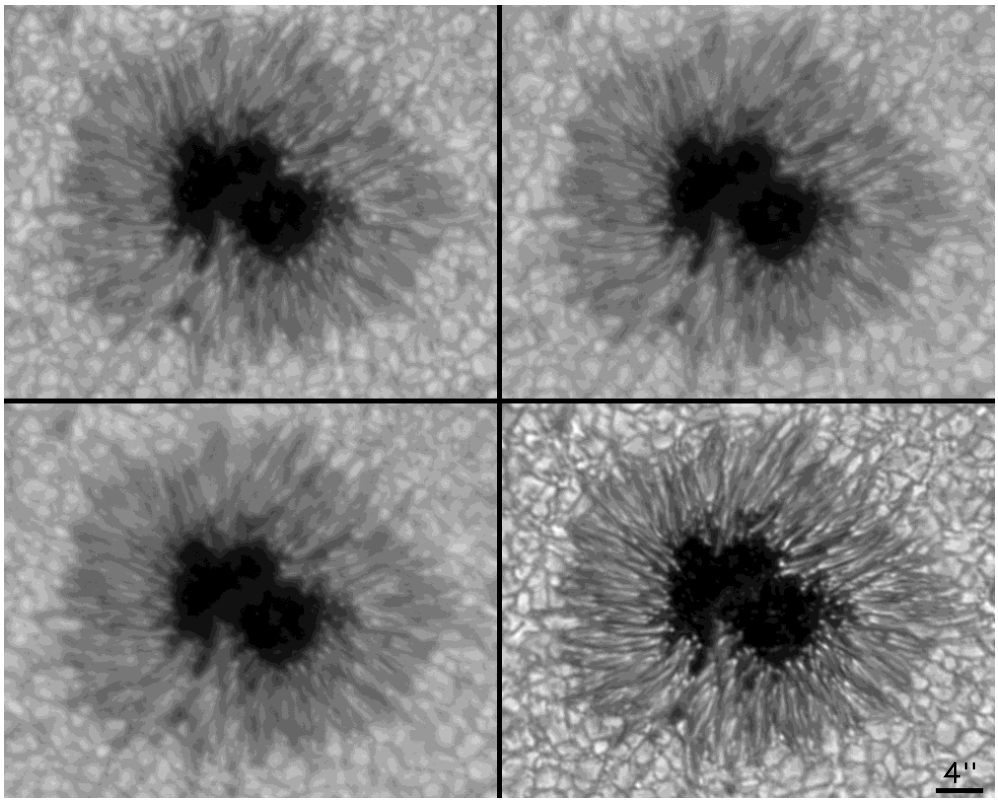

Fig. 1. Sunspot images taken from the sequence at 450.7 nm. *Lower right panel*: central part of the restored image resulting from the combination of three raw images observed close in time and shown in the other three panels of the figure. Each raw image has been individually inverted with phase diversity in order to evaluate its corresponding instantaneous OTF.

the present work (~0.″23), it appears to be formed by narrow, nearly radial bright filaments, separated by dark fibrils. Local brightenings, called penumbral grains (PGs) are observed in the bright filaments. In images of extremely high resolution (better than 0.″12) obtained with the 1-m Swedish Solar Telescope at La Palma, Scharmer et al. (2002) detected dark cores inside the bright filaments.

The magnetic field in the penumbra is as strong as 1500 G at the inner boundary, and decreases to 700 G at the outer boundary, becoming more and more horizontal. In addition, it is very inhomogeneous in the azimuthal direction. From the synthesis of many papers, sometimes presenting conflicting results, it appears that, in the outer penumbra, higher field strengths tend to be correlated with more horizontal fields (by 10 to 20 degrees) and dark intensity structures (see e.g. Beckers & Schröter 1969; Westendorp Plaza et al. 2001; Bellot Rubio 2003, and references therein). In addition to that, several authors report that the magnetic radius of sunspots extends beyond the visible boundary of the penumbra (Skumanich 1992; Title et al. 1993; Martínez Pillet 1997; Westendorp Plaza et al. 2001; Bellot Rubio 2003).

The penumbra of sunspots is not only a magnetic, but also a very dynamic plasma: the bright PGs and dark features both move, either toward or away from the umbra; an irregular and not steady outflow of gas (the Evershed effect) is detected. In the inner penumbra, the PGs always move towards the umbra, and reach a maximum velocity of 0.5 $\mathrm{km\,s^{-1}}$ at the umbra-penumbra boundary (Muller 1973). In the outer penumbra, they have been found to move either towards the surrounding photosphere (Wang & Zirin 1992; Denker 1998; Sobotka et al. 1999; Sobotka & Sütterlin 2001), or towards the umbra (Muller 1973; Tönjes & Wöhl 1982; Zirin & Wang 1989). The dividing line, separating the two opposite motions, is located near the outer boundary at about 1/3 of the width of the penumbra. Schlichenmaier (2002) elaborated a moving flux tube model developing waves and kinks (a photospheric "serpent") that reproduces both directions of motions of the PGs.

The present paper is the first in a series based on two excellent 2-hour time series of sunspot images reconstructed with the phase-diversity technique. The long duration of these series, together with the high and stable quality throughout the whole period, which is substantially improved after the reconstruction (see Fig. 1), makes this material one of the best data sets ever produced to study the morphology and the dynamical behaviour of a sunspots fine structure and its surroundings. In addition, the strict simultaneity of the images in the *G*-band and the blue continuum significantly increases the reliability of the identification and tracking of *G*-band bright points.

In this work we are interested in the relation between the penumbral and the photospheric features as they move across the boundary of a decaying sunspot. Such a decaying sunspot is well suited for our purpose, because it has a simple, nearly symmetric configuration, surrounded by a well developed and nearly circular moat. Moreover, the features in the outer penumbra and in the moat move in the same direction, outward, which is a favourable situation to find out if there is a

continuity in their properties. In the second paper of the series, we will investigate in detail the motions of granules, families of granules formed by recurrently splitting granules, and small-scale magnetic bright points, in order to see how they behave and interact when they are dragged by a supergranular convective flow.

2. Observations and data processing

2.1. Observations

The leading sunspot of a decaying bipolar group NOAA 8620 was observed on 7 July 1999 at the Swedish Vacuum Solar Telescope, La Palma (Scharmer et al. 1985), near the center of the solar disc at $\mu = 0.93$. The sunspot showed a regular shape and a slow and smooth area decay from July 3 to July 13 as recorded in the daily area values of Solar Geophysical Data.

Two strictly simultaneous time sequences of high-resolution images were taken in the wavelength bands at 450.7 ± 0.45 nm (blue) and 430.8 ± 0.55 nm (*G*-band). The observing sequence spans for more than two hours (1282 images per series), from 7:30 UT to 9:43 UT. The images were acquired using two Kodak Megaplus 1.6 CCD cameras, with a dynamical range of 10 bit and 1536 × 1032 pixels. The pixel size and exposure time were 0.″083 and ∼40 ms, respectively. The cameras were placed in orthogonal light paths produced by a cubic beam splitter. A common mechanical shutter in front of the beam splitter ensured the simultaneous exposure in both cameras.

To apply the phase-diversity technique for image reconstruction, pairs of focused and intentionally defocused images must be taken simultaneously. To that aim each CCD camera is equipped with a special beam-splitter that images the focused-defocused image pair onto the same chip (see Fig. 2 in Löfdahl et al. 1998). The defocus is caused by a slightly longer optical path length in one of the split beams. In the present case, the equivalent defocusing displacement in vacuum was 8.85 mm that corresponds to a phase shift at the edge of the aperture of 1.15 waves and 1.10 waves at 430.8 nm and 450.7 nm, respectively. After selection of the common area in both images of the pair, the removal of spurious effects induced by the beam splitter, and by the apodization during restoration process at the edges of the image, the effective field-of-view results in 46″ × 75″ (560 × 910 pixels). The cameras were working in a real-time frame-selection mode storing the best 4 images within a time interval of 18 s. Considering the additional time to transfer the data to the hard disc, the resulting mean time interval between two consecutive sets of 4 images was 25 s.

In an independent third channel, a complementary data set was acquired in the Ca II K line (λ 393.3 ± 0.15 nm) for monitoring the magnetic activity in the observed field. Standard flat-field and dark-current corrections were applied to all images before the image restoration.

2.2. Data processing

As mentioned above, the phase-diversity (PD) technique has been applied to correct the images of the blue and *G*-band sequence up to close the diffraction limit. This technique allows one to estimate both the unknown observed object and the wavefront aberration. A few papers in the literature are complementary in the description of the PD technique for image reconstruction (e.g. Gonsalves & Childlaw 1979; Gonsalves 1982; Paxman et al. 1992; Löfdahl & Scharmer 1994; Paxman et al. 1996). However, we summarize the most relevant items of the method as an introduction to this powerful tool for high resolution solar imaging and to report on our particular setting of parameters and assumptions to run the computing code.

This technique requires the detection of at least two images of the object. One of these is the conventional focal-plane image that is degraded by unknown aberrations induced by the atmosphere and the telescope. The other one is a simultaneous image affected by the same unknown aberrations plus an extra known aberration (the easiest controlled aberration to produce is a defocus). Both image realizations, $i_1(\boldsymbol{q})$ and $i_2(\boldsymbol{q})$, can be mathematically represented by the system of equations

$$\left.\begin{aligned} i_1(\boldsymbol{q}) &= i_0(\boldsymbol{q}) * s_1(\boldsymbol{q}) + n_1(\boldsymbol{q}), \\ i_2(\boldsymbol{q}) &= i_0(\boldsymbol{q}) * s_2(\boldsymbol{q}) + n_2(\boldsymbol{q}), \end{aligned}\right\} \tag{1}$$

where $*$ stands for convolution and $\boldsymbol{q}$ is the vectorial notation for the coordinates of the image points; i_0 is the "true" object and i_1, i_2 are the two observed images; s_1 and s_2 represent the corresponding point spread functions (PSF) of the optical transmission system – including the terrestrial atmosphere and the telescope – and n_1, n_2 are additive terms of noise.

Gonsalves & Childlaw (1979) propose the solution of this system of equations as a least-squares fit which in the Fourier domain can be written as the following error metric:

$$\begin{aligned} L(I_0, S_1) \;=\; \sum_{\boldsymbol{u}} \Big\{ & \Big| I_1(\boldsymbol{u}) - I_0(\boldsymbol{u}) S_1(\boldsymbol{u}) \Big|^2 \\ & + \gamma \Big| I_2(\boldsymbol{u}) - I_0(\boldsymbol{u}) S_2(\boldsymbol{u}) \Big|^2 \Big\}, \end{aligned} \tag{2}$$

where capital letters represent the Fourier transform of the corresponding functions denoted by lower-case characters and $\boldsymbol{u}$ is the frequency vector in the Fourier domain. γ is included as a factor to equalize the noise in both images (a ratio of the respective noise variances). Typical values for noise level in our data at both wavelengths are in the range 0.6–0.8% of the average intensity. S represents the optical transfer function (OTF). It is directly related to the phase aberration in the pupil (see e.g. Bonet 1999), which in turn can be approximated by the first J terms of a Zernike expansion. In the present case Zernike modes 2–21 have been employed in the expansion, i.e. 20 coefficients, $\boldsymbol{\alpha} \equiv \{\alpha_j, j = 2, ..., 21\}$ have to be determined to estimate the wave front error and subsequently $S(\boldsymbol{u}, \boldsymbol{\alpha})$. Using a greater number of modes, e.g. $J = 45$, did not significantly improve the results while it substantially increased the computing time.

Part of the minimization of (2) can be performed analytically. The solution of equation: $\partial L / \partial I_0 = 0$, gives an estimate of the object, $\hat{I}_0$, that minimizes (2) for fixed $\boldsymbol{\alpha}$.

$$\hat{I}_0(\boldsymbol{u}) = \frac{I_1(\boldsymbol{u})\, S_1^*(\boldsymbol{u}, \boldsymbol{\alpha}) + \gamma\, I_2(\boldsymbol{u})\, S_2^*(\boldsymbol{u}, \boldsymbol{\alpha})}{|S_1(\boldsymbol{u}, \boldsymbol{\alpha})|^2 + \gamma\, |S_2(\boldsymbol{u}, \boldsymbol{\alpha})|^2}. \tag{3}$$

The subsequent substitution in (2) leads to the modified error metric $L_M(\boldsymbol{\alpha})$

$$L_M(\boldsymbol{\alpha}) = \sum_{\boldsymbol{u}} \frac{\left|I_1(\boldsymbol{u})\, S_2(\boldsymbol{u},\boldsymbol{\alpha}) - I_2(\boldsymbol{u})\, S_1(\boldsymbol{u},\boldsymbol{\alpha})\right|^2}{|S_1(\boldsymbol{u},\boldsymbol{\alpha})|^2 + \gamma\,|S_2(\boldsymbol{u},\boldsymbol{\alpha})|^2}, \tag{4}$$

which is now independent of the object Fourier transform I_0. Thus, the parameter space over which the optimization is performed has dimension 20. Once these parameters are determined, $\hat{S}_1$ and $\hat{S}_2$ can be constructed and the object estimate, $\hat{I}_0$, can be derived from (3), thereby completing the image reconstruction process.

Poor seeing may produce a low signal-to-noise ratio and very small and uncertain values of $S(\boldsymbol{u})$ at certain spatial frequencies. At these frequencies, Eq. (3) produces an excessive amplification of the signal, giving rise to artifacts that show up as a regular pattern in the restored scene. To circumvent this problem, we combine in a sort of speckle summation (see e.g. Paxman et al. 1996) the results of the inversion of 3 or 4 image pairs taken close in time, so that evolutionary aspects in the solar structures can be neglected. The lower right panel of Fig. 1 shows the central part ($41\farcs5 \times 33\farcs2$) of the final restored image resulting from the combination of three single-image inversions of the blue sequence. These images were recorded within a period of 18 s.

The restored images were de-rotated to compensate for rotation of the field of view in the focal plane induced by the alt-azimuthal configuration of the telescope. Furthermore, the images were aligned, destretched (computer code by Molowny-Horas & Yi 1994), and filtered for p-modes in the $k-\omega$ space (cut-off phase velocity 5 km s^{-1}). Two movies were produced, for the blue continuum and the *G*-band, of 288 frames each, spanning over 2 h (Δt = 25 s) and covering a field of $46'' \times 75''$, with the sunspot located in the center. Direct inspection of the images reveals structures up to about the Rayleigh resolution limit at both working wavelengths (~$0\farcs23$).

A feature-tracking technique (Sobotka et al. 1997) was used to measure positions, intensities and sizes of PGs and of *G*-band bright points. PGs were tracked in the series of blue images. To isolate them from other structures, photospheric granules and umbral dots were masked out and a segmentation algorithm was applied to each blue image, based on the rule that pixels with downward concavity, representing bright features, are set to 1 and the rest to 0 (cf. Sobotka & Sütterlin 2001). The obtained binary masks were then multiplied by corresponding blue images, so that original intensities of PGs were preserved.

To isolate *G*-band bright points, the destretch algorithm was applied to each blue image to align it exactly with the structures in the corresponding *G*-band frame. The granular contrast of aligned blue images was reduced by a factor of 0.833 to match the contrast observed in the *G*-band frames. Then the blue frames were subtracted from the *G*-band frames, thus producing intensity difference images with the *G*-band bright points substantially enhanced. The segmentation was done by thresholding these difference images, obtaining binary masks, and by multiplying the masks by the original *G*-band frames.

After the segmentation, the features under study (PGs and *G*-band bright points) are formed from the non-zero intensity pixels. In the next step, pixels forming a feature are labelled by an identification number. Then, the spatial coincidences of features in each pair of subsequent images are investigated. Two features are identified as predecessor/successor if they coincide in the coordinates of at least one pixel in both frames. The maximum intensity, its coordinates and the total number of pixels in the feature are recorded for each frame. The lifetimes (number of frames) and the sizes (number of pixels) of the features can be obtained directly from the records. Formation, death, splitting and merging of features are taken into account. In the case of splitting, the brightest feature is adopted as the successor, while if merging occurs, the merged feature is defined to be the continuation of the feature with the longest record.

To improve the reliability of the tracking results and to avoid small-scale noise in the segmented images, for the further analysis we select only features with lifetimes and time-averaged sizes above certain minimum values (see Sect. 3), where the minimum size is usually derived from the resolution limit of the observations. Variable image quality may cause spurious merging and splitting that can make independent features appear related. This would lead to large displacements of the maximum intensity positions and to unrealistic velocities of proper motions. This problem can be partially fixed by selection of features with time-averaged velocities smaller than the cut-off velocity used in the $k-\omega$ filter. Time-averaged velocities are calculated using linear least-squares fits to the positions. More additional criteria can be applied to select features with specific characteristics.

Finally, a "visual consistency check" is applied to the selected features: trajectories are checked visually to eliminate discontinuities in position or strong bends/breaks in the trajectory, caused by spurious coincidences of different features, and to discard such features that are not the subject of the study.

3. Results

3.1. Outward-moving penumbral grains

We have already mentioned in Sect. 1 that in the outer 1/3 of the penumbra most of the PGs move towards the outer penumbral border (P/G boundary).

A natural question is what happens when they reach the boundary between the penumbra and the surrounding photospheric granulation (P/G boundary). A visual inspection of a movie composed of the blue images shows that the outward-moving PGs evolve in three possible ways:

1. They disappear in the penumbra before reaching the P/G boundary.
2. They cross the P/G boundary and continue to move in the granulation as small bright features.
3. After crossing the P/G boundary, they increase their size and develop into granules that move away from the sunspot.

This different behaviour of the PGs crossing the P/G boundary is quite remarkable and justifies the separate study of the features that are observed to expand and those that do not expand.

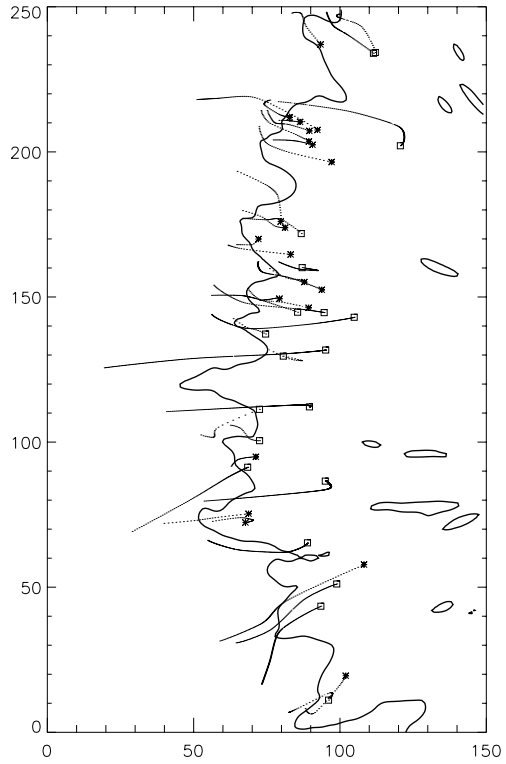

Fig. 2. Trajectories of PGs that crossed the P/G boundary, approximated in the figure by a time-averaged contour. Origins of trajectories are marked by asterisks for small features and by squares for granules. The coordinate unit is 1 pixel, i.e., 0.″083.

To study the evolution of PGs quantitatively, the mentioned above feature-tracking technique was applied to a field of 12.″5 × 20.″8, including a part of the penumbra and adjacent granulation. This region is located on the left-hand side of the sunspot in Fig. 1 (see also Fig. 2 showing the contour of the time-averaged outer penumbral border in this region). The criteria to select bright features of interest from the raw results of the tracking (see Sect. 2) were as follows: (a) minimum lifetime of 250 s, making it possible to pass a distance of 1000 km with the (b) maximum allowed average speed of 4 km s^{-1}; (c) minimum average size of 0.″28, corresponding to an area of 9 pixels. To eliminate from the tracking results most of the granules and PGs that probably do not cross the P/G boundary, an additional criterion (d) of average brightness ranging from $I = 0.9$ to 1.15 (in units of the mean photospheric intensity) was applied. This criterion was derived from the histogram of time-averaged intensities (resulting from the tracking), which clearly showed two populations, PGs and granules, with peaks at $I = 0.92$ and 1.16, respectively, and with a dip at $I = 1.02$. We can expect that the time-averaged intensities of PGs that cross the P/G border and penetrate into the granulation correspond to the overlap of both populations. This way, 712 bright features were selected. Finally, the visual consistency check was applied to these features and all inward moving PGs, together with features originating outside the penumbra were discarded.

After the visual consistency check we obtained a sample of 126 outward moving PGs, including their trajectories. The noise in the measured positions was removed by smoothing the trajectories using cubic splines. Instantaneous velocities were calculated as derivatives of the smoothed trajectories. Each PG was inspected individually to check its positions in time with respect to the P/G boundary. About 2/3 of PGs disappear before reaching the P/G boundary, 1/6 cross the boundary and continue moving as small bright features with a diameter less than 0.″5, and about 1/6 cross the boundary, expand in size, and develop into granules – here we use the term granules because the visual inspection of the movie reveals that these structures, when present in the photosphere, do behave as normal granules. All the features that cross the P/G boundary preserve their outward motion. Their trajectories, smoothed by cubic splines, are plotted in Fig. 2 together with the time-averaged contour of the P/G border. This contour is shown only for illustration, because the ragged border of the penumbra evolves in time and only individual tracking of PGs gives the information if they crossed the P/G boundary or not. The origins of trajectories are marked by asterisks for small features and by squares for granules. Dots denote the following positions; in the case of slow motions the dots merge, forming solid lines. In general, the birth places of crossing and non-crossing PGs are mixed. However, on average, crossing PGs in our sample originate at the distance of about 2″ from the P/G boundary while the non-crossing ones by 0.″9 deeper in the penumbra (the width of the penumbra is approximately 8″–10″). The present sample of PGs does not include all PGs in the field of view.

The total lifetimes (including the penumbral and photospheric stages) of the PGs that convert into small bright features are in the range of 4.6–41.0 min with the mean of 13.9 min. The total lifetimes of the PGs that develop into granules are longer: 5.9–120.0 min, with an average of 36.0 min. For comparison, the non-crossing PGs live 4.2–102.5 min, with a mean lifetime of 14.3 min. After crossing the penumbral border, small features have lifetimes in the range 2.5–22.1 min with the mean of 7.7 min. For granules which arise from PGs, the range is 1.7–36.3 min and the mean is 15.0 min. Alissandrakis et al. (1987) give a mean lifetime of photospheric granules of 16 min. Hence, after crossing the border, granules of penumbral origin have a mean lifetime comparable with granules formed in the quiet photosphere. Small features live shorter than "average" granules but longer than small (<0.″5) ones, with a lifetime that was estimated at 1–3 min (Kawaguchi 1980; Hirzberger et al. 1999).

The lifetime-averaged speeds of small bright features range from 0.4 to 2.7 km s^{-1} with a mean of 1.4 km s^{-1}. The newly formed granules are slower: 0.2–1.9 km s^{-1}, with a mean speed of 1.1 km s^{-1}. These velocities are slightly higher compared to the average speed of all outward moving PGs near the P/G border (0.9 km s^{-1}, Sobotka & Sütterlin 2001) and to the horizontal speed of granules close to sunspots (0.5–0.8 km s^{-1}, Muller & Ména 1987; Simon et al. 1988).

Figure 3 demonstrates the transformation of an outward moving PG into a small bright photospheric feature (*top*) and into a granule (*bottom*). Dark dots in the figure denote intensity maxima of the features.

In Table 1 we summarize the numbers of PGs that disappear in the penumbra before crossing the P/G boundary, PGs that

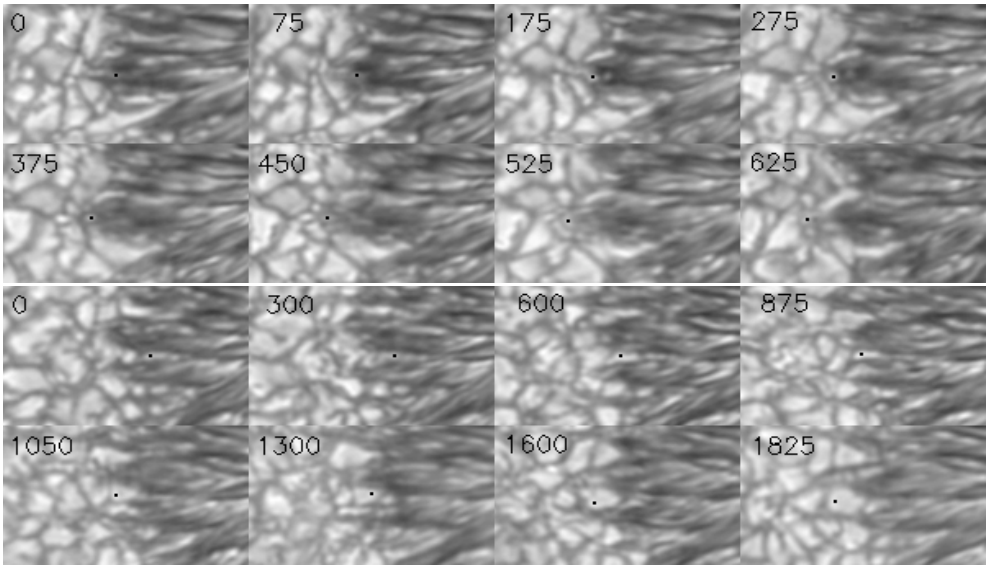

Fig. 3. Series of frames showing two examples of PGs crossing the P/G boundary and converting into a small bright feature (*top*) and into a granule (*bottom*). The tracked features are marked by small black dots at the positions of intensity maxima. Numbers in the upper left corners show the elapsed time in seconds. The field of view is $12\farcs5 \times 7\farcs5$.

Table 1. Summary of PGs near the P/G border.

PGs	Total number	Accel.	Decel.
Non-crossing	85 (67%)		
→ Small features	21 (17%)	6	13
→ Granules	20 (16%)	11	6

cross the P/G border and convert into small bright photospheric features, and those that develop into granules. We also show the numbers of PGs that accelerate or decelerate their motion before and during the crossing of the boundary. Note that most of the PGs which convert into small features decelerate before they escape from the penumbra, while those that expand and develop into granules accelerate.

3.2. Relation of G-band bright points to the penumbra

Numerous *G*-band bright points were observed in the sunspot moat, which, in our case, had approximately an annular shape and an average width of 8″. This has been determined from the horizontal velocity field of granules around the spot. The details will be described in the second paper of this series. The feature tracking algorithm was applied to the series of segmented *G*-band frames, detecting 776 *G*-band bright points with lifetimes longer than 2.5 min and with time-averaged sizes larger than $0\farcs28$. Most of the *G*-band bright points (95%) move away from the sunspot. A detailed analysis of their trajectories and horizontal velocities will be published in the second paper of this series.

To find a possible relation of the *G*-band bright points with the penumbra and penumbral features, we looked for such *G*-band bright points that were born in the neighbourhood of the penumbral border. The neighbourhood was defined by the maximum distance of $0\farcs25$ (3 pixels) between the birth position of the *G*-band bright point and the nearest penumbral feature, i.e., PG or a dark penumbral area or a dark fibril. The distance of 3 pixels is comparable with the Rayleigh's resolution limit ($0\farcs23$) of a diffraction-limited 47.5 cm telescope at 430 nm. The birth positions of 776 *G*-band bright points, obtained from the feature tracking, were compared visually (see examples in Fig. 4) with the locations of penumbral features in the aligned blue images (Sect. 2). The blue wavelength band

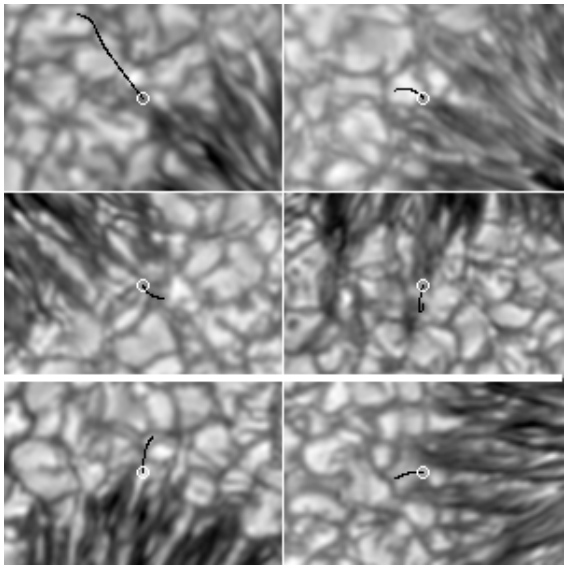

Fig. 4. Blue continuum images showing the birth positions of four *G*-band bright points (*top*) born near the tips of dark penumbral fibrils and two (*bottom*) in the vicinity of bright PGs. *G*-band bright points are not evident in the blue continuum so that they are represented by white circles with radii $0\farcs25$ marking their initial positions and by black lines representing their trajectories. The field of view in the images is $12\farcs5 \times 8\farcs3$.

was selected because of higher contrast. In total, we found 191 *G*-band bright points born in the neighbourhood with the penumbra and then drifting away from the spot. Most of them, 132 (69%), originate in the vicinity of dark penumbral areas or fibrils, where the magnetic field is expected to be stronger and more horizontal than in bright filaments. Very often, the *G*-band bright points are born on the tips (ends) of dark penumbral fibrils. Thus, in the vicinity of a decaying sunspot, most of the *G*-band bright points, which are believed to be associated with thin magnetic flux tubes, appear to be born close to a magnetized plasma. Only 59 (31%) *G*-band bright points appear near bright penumbral features (PGs or bright filaments) or close to diffuse regions in the penumbra, which are difficult to classify as "dark" or "bright". Figure 4 represents blue continuum images showing the birth positions of six *G*-band bright points. Since they are not *G*-band images the bright points are not evident in the figure and, consequently, white circles – with the radius of 0.″25 – are employed to indicate their initial positions or equivalently to outline their neighbourhood. Black lines represent trajectories of the bright points' motions. Four of these *G*-band bright points were born on the tips of dark penumbral fibrils and two in the vicinity of bright PGs.

The small bright features escaping from the penumbra and the *G*-band bright points born close to the P/G boundary are, at first sight, similar in morphology and dynamics. To check for possible coincidences between them, we compared, frame by frame, the positions of PGs after crossing the P/G border with the positions of all *G*-band bright points. We did not find any case of coincidence in time and position, so that we can conclude that escaped PGs and *G*-band bright points are different types of features and that *G*-band bright points that are located near the P/G boundary do not originate from bright features which crossed the P/G boundary.

In quiet granulation, *G*-band bright points usually appear in dark spaces which are compressed by expansion or convergent motions of neighbouring granules (Muller 1983; Muller et al. 1989; Muller & Roudier 1992). Inspecting the *G*-band movie, we observe that in 95% of all cases, the formation of *G*-band bright points in the neighbourhood of the penumbral border also occurs in areas compressed by convergent horizontal motions caused by outward moving penumbral features and expanding granules adjacent to the border. In quiet granulation, the formation of *G*-band bright points can be attributed to the concentration of diffuse magnetic flux, already present in the intergranular space, by converging or expanding adjacent granules. A similar mechanism of concentration of magnetic flux could also take place in the magnetic penumbral plasma at the P/G border.

4. Discussion and conclusions

Two time series of 288 frames each, spanning over two hours and taken simultaneously in the *G*-band and the blue continuum were restored for instrumental and atmospheric degradation using the phase-diversity technique. The excellent quality of the restored images and the stability with time made it possible to study relations between small-scale penumbral and photospheric features near the outer penumbral boundary: PGs, dark penumbral fibrils, granules, and *G*-band bright points.

It was shown that about 1/3 of outward moving PGs located near the outer penumbral boundary escape from the penumbra and penetrate into the surrounding granulation where they continue their outward motion, either as small bright features, or growing as expanding granules. Their velocities are slightly higher than average speeds in the outer penumbra and in the sunspot moat. They do not evolve as *G*-band bright points in the sense that the PGs escaping from the penumbra never coincide spatially with the *G*-band bright points that are located near the P/G boundary.

While some PGs, belonging to the less-magnetized component in the penumbra, convert into presumably non-magnetic or weakly magnetized granules, many *G*-band bright points are born close to dark penumbral fibrils (or directly at their tips), where the magnetic field is strong and nearly horizontal. This confirms the finding by Title et al. (1995) and Shine et al. (1996), reported by Ryutova et al. (1998), that "moving magnetic features" frequently appear along the continuation of dark filaments. In addition, our observations show that local convergent motions, caused by the expansion of granules and outward moving penumbral features, may play a role in their formation. The compression of a dark space by the surrounding granules, either in the photosphere away from sunspots, or at the sunspot border, should be accompanied by a strong downflow, which may help to concentrate the flux into a magnetic flux tube, detected as a moving magnetic feature or a *G*-band bright point. It would be of much interest to obtain high spatial resolution spectra simultaneously with *G*-band images, to check whether the formation of *G*-band bright points is associated with strong downflows in dark filaments at the P/G border of sunspots.

We have not found in the literature any sunspot penumbra model able to explain our observations.

Acknowledgements. J.A.B. and I.M. are grateful to M. G. Löfdahl for providing his original PPDS source code in ANA and for his advice in the construction of the IDL code basis of the present work. M.S. and J.A.B. thank the Paul Sabbatier University in Toulouse for the stay at the Pic du Midi Observatory. R.M. and M.S. thank I.A.C. for hospitality. The Swedish Vacuum Solar Telescope was operated on the island of La Palma by the Royal Swedish Academy of Sciences at the Spanish Observatorio del Roque de los Muchachos of the Instituto de Astrofísica de Canarias. The support provided by R. Kever and G. Hosinsky during the observations is gratefuly acknowledged. Partial support by the Spanish Ministerio de Ciencia y Tecnología and by FEDER through project AYA2001-1649 is gratefully acknowledged. A part of this work was done in the framework of the research projects IAA3003404 and K2043105 of the Academy of Sciences of the Czech Republic and of the project 205/01/0658 of the Grant Agency of the Czech Republic. Part of this work has been supported by the *Deutsche Forschungsgemeinschaft* under grant PE 782/4 (AT). This research is part of the European Solar Magnetism Network (EC contract HPRN-CT-2002-00313).

References

Alissandrakis, C. E., Dialetis, D., & Tsiropoula, G. 1987, A&A, 174, 275

Beckers, J. M., & Schröter, E. H. 1969, Sol. Phys., 4, 303

Bellot Rubio, L. 2003, in 3rd international workshop on solar polarization, ed. J. Trujillo Bueno, & J. Sánchez Almeida, ASP Conf. Ser., 307, 302
Bonet, J. A. 1999, in Motions in the solar atmosphere, ed. A. Hanslmeier, & M. Messerotti, ASSL Ser., 239 (Dordrecht: Kluwer), 1
Brickhouse, N. S., & La Bonte, B. J. 1988, Sol. Phys., 115, 43
Denker, C. 1998, Sol. Phys., 180, 81
Gonsalves, R. A., & Childlaw, R. 1979, in Applications of digital image processing III, ed. A. G. Tescher, Proc. Soc. Photo-Opt. Instrum. Eng., 207, 32
Gonsalves, R. A. 1982, Opt. Eng., 21, 829
Harvey, K., & Harvey, J. 1973, Sol. Phys., 28, 61
Hirzberger, J., Bonet, J. A., Vázquez, M., & Hanslmeier, A. 1999, ApJ, 515, 441
Kawaguchi, I. 1980, Sol. Phys., 65, 207
Lee, J. W. 1992, Sol. Phys., 139, 267
Löfdahl, M. G., & Scharmer, G. B. 1994, A&AS, 107, 243
Löfdahl, M. G., Berger, T. E., Shine, R. S., & Title, A. M. 1998, ApJ, 495, 965
Martínez Pillet, V. 1997, in Advances in the physics of sunspots, ed. B. Schmieder, J. C. del Toro Iniesta, M. Vázquez, ASP Conf. Ser., 118, 212
Meyer, F., Schmidt, H. U., Weiss, N. O., & Wilson, P. R. 1974, MNRAS, 169, 35
Molowny-Horas, R., & Yi, Z. 1994, ITA (Oslo) Internal Rep. No. 31
Muller, R. 1973, Sol. Phys., 29, 55
Muller, R. 1983, Sol. Phys., 85, 113
Muller, R., & Ména, B. 1987, Sol. Phys., 112, 295
Muller, R., & Roudier, T. 1992, Sol. Phys., 141, 27
Muller, R., Hulot, J. C., & Roudier, T. 1989, Sol. Phys., 119, 229
Paxman, R. G., Schulz, T. J., & Fienup, J. R. 1992, J. Opt. Soc. Am. A9, 7, 1072
Paxman, R. G., Seldin, J. H., Löfdahl, M. G., Scharmer, G. B., & Keller, C. U. 1996, ApJ, 466, 1087
Petrovay, K., & Moreno-Insertis, F. 1997, ApJ, 485, 398
Ryutova, M., Shine, R. A., Title, A. M., & Sakai, J. I. 1998, ApJ, 492, 402
Scharmer, G. B., Brown, D. S., Petterson, L., & Rehn, J. 1985, Appl. Opt., 24, 2558
Scharmer, G. B., Gudiksen, B. V., Kiselman, D., Löfdahl, M. G., & Rouppe van der Voort, L. H. M. 2002, Nature, 420, 151
Schlichenmaier, R. 2002, Astron. Nachr./AN, 323, 303
Sheeley, N. R. 1969, Sol. Phys., 9, 347
Sheeley, N. R. 1972, Sol. Phys., 25, 98
Sheeley, N. R., & Bhatnagar, A. 1971, Sol. Phys., 19, 338
Shine, R. A., Title, A. M., Frank, Z. A., & Scharmer, G. 1996, BAAS, 28, 871
Simon, G. W., Title, A. M., Topka, K. P., et al. 1988, ApJ, 327, 964
Skumanich, A. 1992, in Sunspots: Theory and Observations, ed. J. H. Thomas, & N. O. Weiss (Dordrecht: Kluwer), 121
Sobotka, M., Brandt, P. N., & Simon, G. W. 1997, A&A, 328, 682
Sobotka, M., Brandt, P. N., & Simon, G. W. 1999, A&A, 348, 621
Sobotka, M., & Sütterlin, P. 2001, A&A, 380, 714
Title, A. M., Frank, Z. A., Shine, R. A., et al. 1993, ApJ, 403, 780
Title, A. M., Frank, Z. A., Shine, R. A., Tarbell, T. D., & Simon, G. W. 1995, BAAS, 27, 978
Tonjes, K., & Wöhl, H. 1982, Sol. Phys., 78, 63
Vrabec, D. 1971, in Solar magnetic fields, ed. R. Howard (Dordrecht: Reidel), IAU Symp., 43, 329
Vrabec, D. 1974, in Chromospheric fine structure, ed. G. Athay (Dordrecht: Reidel), IAU Symp., 56, 201
Wang, H., & Zirin, H. 1992, Sol. Phys., 140, 41
Westendorp Plaza, C., del Toro Iniesta, J. C., Ruiz Cobo, B., et al. 2001, ApJ, 547, 1130
Zirin, H., & Wang, H. 1989, Sol. Phys., 119, 245